Int. J. Electrochem. Sci., 17 **(2022)** Article Number: 2212101, doi: 10.20964/2022.12.102

International Journal of
ELECTROCHEMICAL
SCIENCE
www.electrochemsci.org

N-doped Carbon Quantum Dots with Mechanical Enhancement and Fluorescence Properties Toward Anti-Corrosion Coating

Zhigang Di[1,*], *Qifeng Zhao*[1], *Hui Xu*[1], *Kang Wu* [1], *Yan Yan*[1], *Xi Jin*[1], *Haiying Shen*[1] *Yiqian Lv*[2], *Boyuan Ran*[3]

[1] CNOOC Changzhou Paint and Coatings Industry Research Institute, Changzhou 213016, China
[2] College of Material Science and Engineering, Beijing University of Chemical Technology, Beijing 100029, China
[3] National Center for Materials Service Safety, University of Science and Technology Beijing, Beijing 100083, China
[*]E-mail: dizhg@cnooc.com.cn (Z. Di)

Received: 9 October 2022 / *Accepted:* 12 November 2022 / *Published:* 27 December 2022

To improve the anti-corrosion performance and mechanical properties of waterborne epoxy, we synthesized new N-CQDs and introduced them into the coating to prepare N-CQDs/EP. Based on SEM, Micro FT-IR, EIS, NSS, adhesion Tester, and LSCM, the long-term corrosion resistance, mechanical, and fluorescence properties of N-CQDs/EP were studied carefully. The cross-sectional SEM results indicated that N-CQDs could improve the internal cross-linking density and reduce the pore size of N-CQDs/EP. EIS results showed that composite coating could provide excellent anti-corrosion to steel in both 3.5 wt% NaCl solution and simulated seawater. The highest impedance value of N-CQDs/EP was still maintained at 10^9 Ω cm^2 after 30 d immersion. N-CQDs also enhanced the adhesion force, and the highest value was 6.8 MPa. Meanwhile, the N-CQDs/EP fluorescence intensity was increased with the appearance of N-CQDs. Hence, this work can provide theoretical support for developing new epoxy coatings and accelerate the industrial application of long-term coatings.

Keywords: Coating, Carbon quantum dots, EIS, Adhesion force, Fluorescence.

1. INTRODUCTION

Steel is widely used in all walks of life because of its excellent strength, plasticity, elasticity, and low price [1-3]. Steel is called the skeleton of industry. With the deep exploitation of marine resources, steel consumption is also surging. Steel is used extensively in manufacturing ships, exploration instruments, and offshore platforms [4]. However, steel equipment is susceptible to corrosion in harsh marine environments, especially in the South China Sea. Unlike other regional corrosion types, corrosion in the South China Sea is highly saline and alternately wet and dry. In addition to causing substantial

economic losses, corrosion can cause serious safety accidents [5, 6]. How to effectively slow down the corrosion rate of metals was a complex problem for researchers. The main anti-corrosion techniques include corrosion inhibitors [7-10], organic coatings [11, 12], internal optimization of metal structures [13], and cathodic protection [14]. Organic coatings are widely used among the above technologies because of their low price, versatility, and variety. In addition, chromates are often added to coatings as reinforcing agents to enhance the corrosion resistance of the coating.

As the awareness of environmental protection increases, toxic and harmful additives are gradually banned [15]. Green and eco-friendly waterborne epoxy coatings have been extensively developed. However, waterborne coatings possess poor mechanical properties in the marine environment, which causes them to blister and peel easily. Microcracks and microporosity are produced in waterborne coatings during service, reducing their corrosion resistance. Researchers generally reinforce waterborne epoxy coatings by introducing additives, such as two-dimensional materials and mesoporous silica. Based on fluorinated rGO and CeO_2, Wu prepared a waterborne epoxy coating with long-term corrosion resistance [16]. Macro and micro electrochemistry analyzed the impact of composite materials in coatings. However, the author ignored that rGO may cause galvanic corrosion after coating damage. Schriver found that the intact coatings with graphene showed excellent corrosion resistance for copper [17]. Unfortunately, galvanic corrosion occurred between graphene and copper after the coating was damaged, thus accelerating the corrosion rate of the copper. Galvanic corrosion also appears on the steel surface. Ding achieved the directional arrangement of GO in the waterborne coating by layer-layer spray to solve this problem [18]. At the same time, the corrosion resistance of the composite coating was also strengthened. By growing ZIF-8 on the GO surface in situ, Li improved GO dispersion and reduced galvanic corrosion probability [19]. Using micro-electrochemistry, Li found that the composite coating possessed reliable self-healing properties. In addition to two-dimensional materials, mesoporous nanosilica is commonly used in composite coatings. Wang introduced 1,10-phenanthroline-5-amine (Phen-NH_2) and cetyltrimethylammonium bromide (CTAB) into mesoporous silica under alkaline conditions and then prepared composite epoxy coatings [20]. EIS results showed that Phen-NH_2 and CTAB enhance the anti-corrosion and self-healing properties of composite coatings.

Nitrogen-doped carbon quantum dots (N-CQDs) contain many advantages, such as good water solubility, excellent optical properties, and eco-friendly [21]. N-CQDs are also superior corrosion inhibitors for steel in different environments. Ren prepared N-doped carbon dots in a hydrothermal reactor with salicylic acid and urea [22]. Then, they explored the anti-corrosion effect of N-CQDs on steel in a harsh solution. Considering the excellent compatibility between carbon quantum dots and epoxy resin, they also possess the potential to be used in epoxy coatings.

Under the hydrothermal reaction at 170 ℃ for 5 h, we prepared new nitrogen-doped carbon quantum dots (N-CQDs) using L-tartaric acid and O-phenylenediamine. Based on the EIS and neutral salt spray test (NSS), the long-term corrosion resistance of the composite coating was studied in depth. In addition to considering the influence of N-CQDs concentrations on the composite coating, we also examined the anti-corrosion performance of the composite coating in natural seawater. Meanwhile, we also studied the impact of various concentrations N-CQDs on coating mechanical properties. Combined with the LSCM, the fluorescence characteristics of the composite coatings were also explored. Finally, we used SEM/EDS to explore the steel morphology change and element distribution. Undoubtedly, this

work can provide theoretical guidance for developing new and efficient epoxy coatings and promote the industrial application of long-term coatings.

2. EXPERIMENTS AND MATERIALS

2.1 Materials

L-tartaric acid (99.99%) and O-phenylenediamine (99.5%) were purchased from Shanghai Aladdin Biochemical Technology Co., LTD, China. Meanwhile, other reagents also came from the same company and were used without further treatment. The simulated seawater contained 23.98 g/L NaCl, 5.029 g/L $MgCl_2$, 4.01 g/L Na_2SO_4, 1.14 g/L $CaCl^2$, 0.699 g/L KCl, 0.172 g/L $NaHCO_3$, 0.100 g/L KBr, 0.0254 g/L H_3BO_3, 0.0143 g/L $SrCl_2$, 0.0029 g/L NaF and deionized water.

The coating metal was Q235 steel obtained from a local dealer. The elements of Q235 steel were 0.22% C, 1.4% Mn, 0.35% Si, 0.05% S, 0.04% P, and 97.94% Fe. The sample size used for electrochemical tests was 1*1*1 cm^3, while the size used for the neutral salt spray test was 10*8*0.2 cm^3.

2.2 Preparation and detection of N-CQDs

2.2.1 Preparation of N-CQDs

The N-CQDs were obtained based on the conventional hydrothermal synthesis method. L-tartaric acid and O-phenylenediamine (weight ratio was 2:3) were added to a 50 ml Teflon liner (with stainless steel shell) and were heated to 170 ℃ for 5 h. The brown solution was cold to room temperature and then purified for 24 h by dialysis bags (1000 Da). Finally, the powder was obtained after rotary evaporation and freeze-drying.

2.2.2 Structural Characterization of N-CQDs

The structure of N-CQDs was identified via Fourier Transform Infrared Spectrometer (FT-IR). The FT-IR acquisition step was 0.5 cm^{-1}, and the wave number range was 4000 cm^{-1} to 500 cm^{-1}. A Transmission Electron Microscope (TEM) was used to study the morphological distribution and size of N-CQDs. The experiment selected copper mesh as the carrier for sample observation. An X-ray diffraction spectrometer (XRD-6100) was used to determine N-CQDs crystal state and morphology. The chemical structure of N-CQDs was tested by a double-beam ultraviolet-visible spectrophotometer (TU-1901).

2.3 Preparation of coating

The additional amounts of N-CQDs in 10 g epoxy coating were 0.01 g, 0.03g, and 0.05g, respectively. To ensure uniform dispersion of N-CQDs in the emulsion, the mixed phase was placed in the blender and ran at 600 r/min for 30 s. The curing agent was added and ran at 600 r/min for 30 s, 1500 r/min for 1 min, and 3500 r/min for 3 min. In this case, the bubble in the coating was removed as much as possible. Under the shear force, the composite coating was coated on the electrode and salt spray sample surface using a 50 um linear coating rod. It should be noted that all substrate for coatings (EP and N-CQDs/EP) in this work was Q235 steel. Then, the prepared coatings on steel were dried at room temperature for one week and were marked as 0.1 N-CQDs/EP, 0.3 N-CQDs/EP, and 0.5 N-CQDs/EP. The same process prepared pure epoxy coating on Q235 steel as the blank control group.

2.4 Characteristics of coating

SEM (S4800, HITACHI) was used to observe different cross-sections to understand the influence of N-CQDs on coatings structure. The fluorescent effect of various coatings was completed by a biological laser scanning confocal microscope (LEICA, TCS SP5). The wavelength of ultraviolet light was λ = 405 nm in this work. Then, the adhesion force between the composite coating and the Q235 steel matrix was tested via the PosiTest AT-M Adhesion tester. Micro-infrared spectroscopy (Micro-FTIR Cary660+620) was used to study the composition changes of EP and composite coatings before and after immersion.

2.5 Anti-corrosion investigation

The anti-corrosion performance of coatings was explored with a three-electrode system containing a working electrode (coating on Q235 steel), a counter electrode (platinum sheet), and a reference electrode (saturated calomel electrode). For the consistency of the results, all the electrochemical tests were completed in Modulab XM, Solartron. The test frequency range was 10^{-2}-10^{5} Hz, and the disturbance signal was 20 mV sine wave.

A 5 cm cross scratch was made on the sample surface with a scalpel, then placed in a neutral salt spray box and photographed regularly. It was worth noting that the concentration of salt mist was 8 wt% NaCl solution.

3. RESULTS AND DISCUSSION

3.1 Performance analysis of N-CQDs

3.1.1 N-CQDs morphology characterization

The XRD spectrum of N-CQDs was shown in Fig. 1a. According to the PDF card query, the diffraction peak of N-CQDs was 2θ =22.032°, and the lattice spacing was 0.403 nm. N-CQDs layer

spacing was significantly greater than that of graphene (0.34 nm), indicating that the introduction of N and O atoms in N-CQDs increased the layer spacing of amorphous carbon compounds.

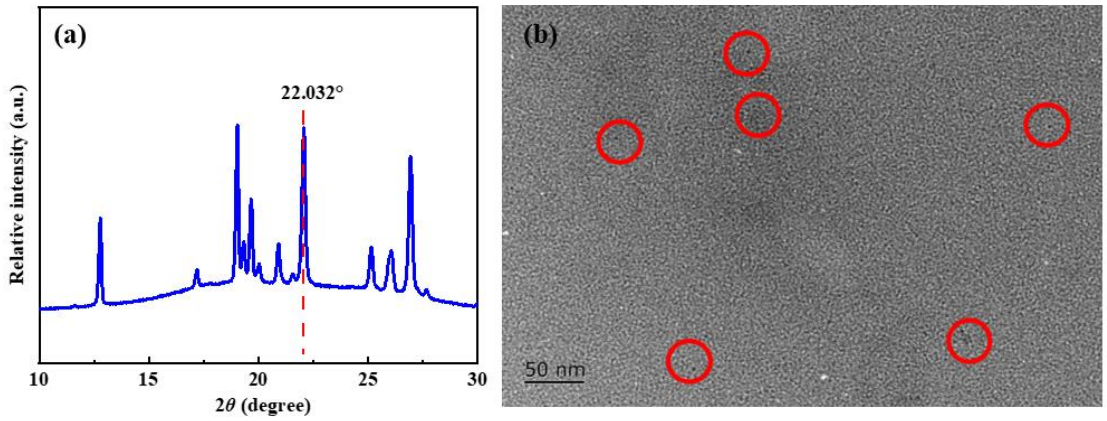

Figure 1. The image of N-CQDs: (a) XRD Spectrum, (b) TEM.

TEM image characterized the morphology and size of N-CQDs, as shown in Fig. 1b. N-CQDs showed an amorphous spherical structure of 2~6 nm. Combined with the characterization of the structure and properties of N-CQDs, it was demonstrated that the carbonized N-CQDs were quantum-sized with good water solubility and fluorescence characteristics. It was worth noting that this was common to all carbon quantum dots.

3.1.2 Structural Analysis of N-CQDs

Fig. 2a showed the UV-Vis and FT-IR spectra of N-CQDs. It could be seen from the FT-IR that the peak at 749 cm^{-1} was caused by the out-of-plane bending vibration of C−H of the benzene ring. The peaks at 3108 cm^{-1} and 1461 cm^{-1} stood for −NH/−OH and C−N stretching, respectively [23]. The characteristic peaks of C=O and C−O stretching vibration were located at 1617 cm^{-1} and 1223 cm^{-1}. It could be seen in Fig. 2b that the absorption characteristic peaks of N-CQDs were located at 270 nm and 322 nm. The 270 nm absorption peak was due to the π-π* transition of the conjugated structure, while the 322 nm peak was the n-π* electronic transition caused by the C=N bond in N-CDs.

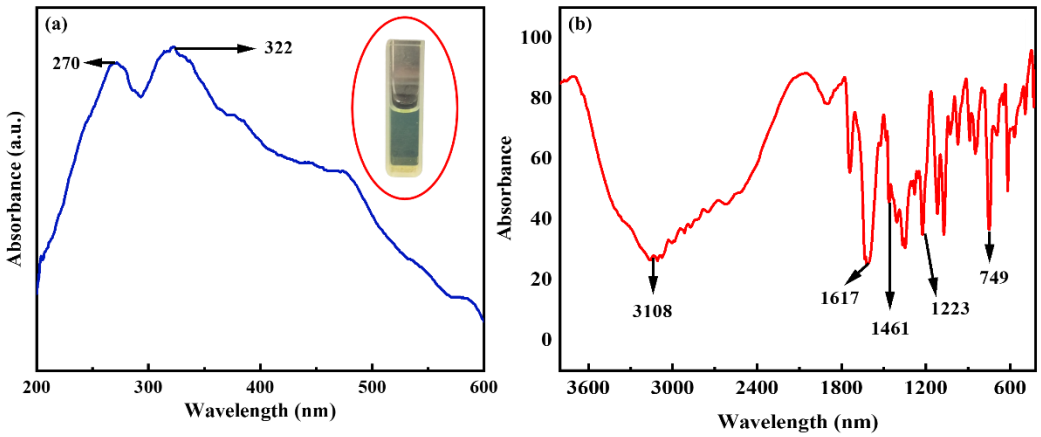

Figure 2. UV-Vis and FT-IR spectra of N-CQDs: (a) UV-Vis, (b) FT-IR.

3.2 The characteristics of coatings

The cross-sectional morphologies of EP and 0.3 N-CQDs were shown in Fig. 3. As shown in Fig. 3a, various pores and cracks were observed inside the pure EP, implying weak barrier performances. In other words, the corrosion media (H_2O, Cl^- ions) could quickly reach and corrode the metal through holes and cracks. The cross-sectional morphology of 0.3 N-CQDs/EP was compact, and no apparent holes and cracks were found in Fig. 3b. This result indicated that the N-CQDs could improve the cross-linking points and cross-linking density of the resin and reduce the pore size of the cross-linking network [24]. In this case, it is difficult for the corrosion media to reach the metal surface through the composite coating.

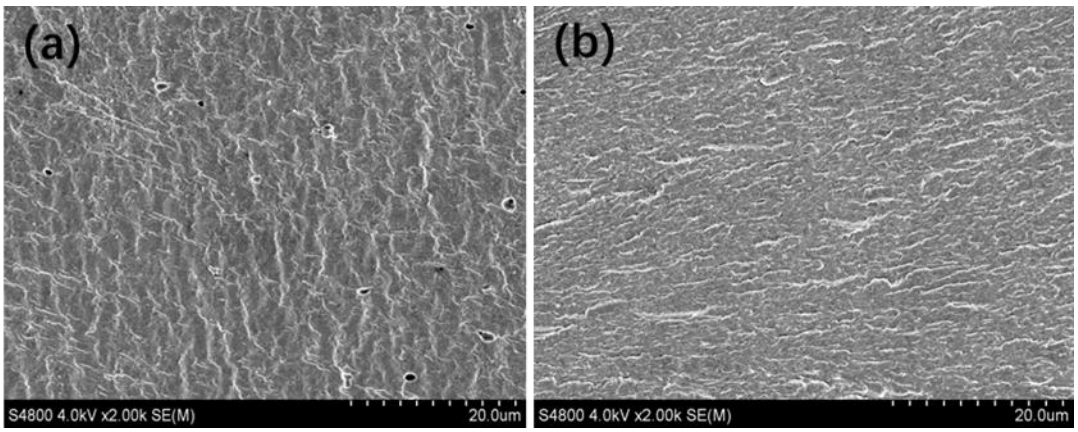

Figure 3. The cross-sectional morphologies of EP and 0.3 N-CQDs/EP.

Microscopic infrared testing was further used to explore the subtle changes in the interior of coatings before and after service, which was displayed in Fig. 4. The prominent peaks of the epoxy coating included the stretching vibration peaks of $-CH_3$ (2955.1 cm^{-1} and 2875.5 cm^{-1}), the stretching vibration peak of C=O (1742.9 cm^{-1}), and the epoxy based characteristic peak (910.2 cm^{-1}). Compared

with the 0 d and 30 d FT-IR spectra of EP, there was no noticeable change in the position and intensity of peaks. These phenomena indicated that the pure EP surface structure and chemical composition were consistent after 30 d immersion. Moreover, no molecular chain breakage was seen in Fig. 4a, indicating that the epoxy coating was intact. N-CQDs/EP coating on steel (Fig. 4b) exhibited the same result as EP, which stated that N-CQDs/EP structure was also unchanged. It was worth noting that the coating on steel still showed water absorption behavior when immersed in NaCl solution.

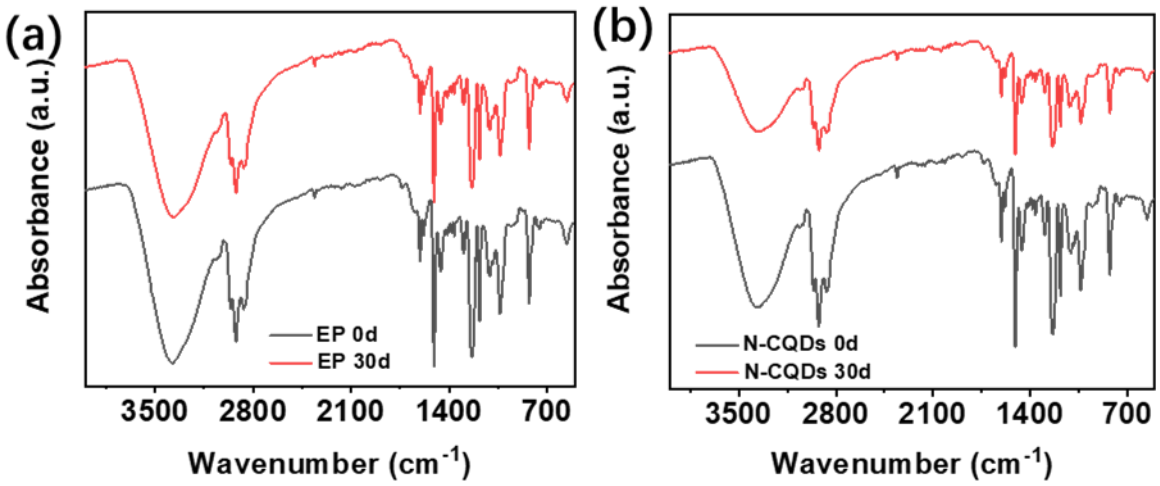

Figure 4. FT-IR spectra of (a) EP and (b) 0. 3 N-CQDs/EP after 0 and 30 d electrochemical test in 3.5 wt% NaCl solution.

3.3 Corrosion resistance analysis

Electrochemical tests were used to investigate the long-term corrosion resistance of the composite coating on steel in 3.5 wt% NaCl solution. As shown in Fig. 5, the low-frequency impedance values of all coatings on steel were maintained at about 10^9 Ω cm^2 at 1 d, which indicated that both EP and N-CQDs/EP coatings on steel exhibited the best corrosion resistance at the beginning of service. The maximum phase angle (about 90°) between 10^5 and 10^2 Hz was also illustrated above fact [25, 26]. Due to the cross-linking density and the physical shielding performance of the coating on steel being improved by N-CQDs (0.1, 0.3, 0.5), the initial low-frequency impedance value of N-CQDs/EP coating on steel was higher than pure EP coating on steel.

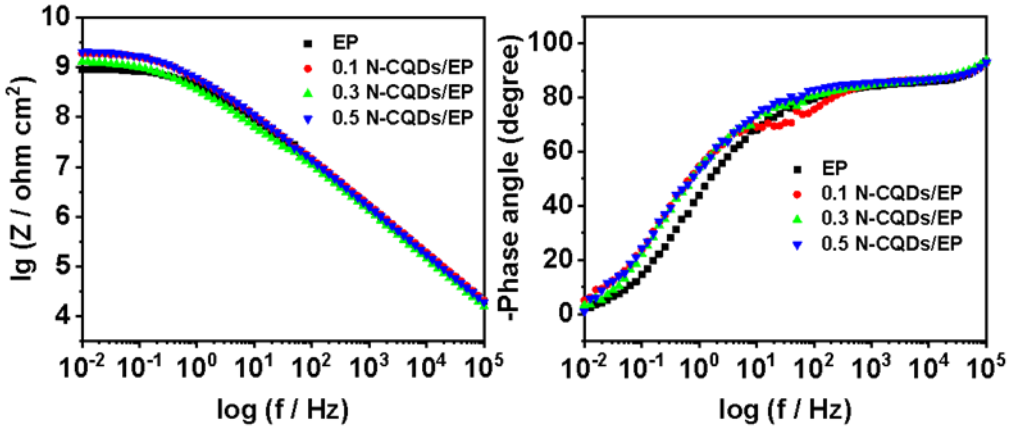

Figure 5. Bode modulus and phase plots of EP and N-CQDs/EP coating on steel immersed in 3.5 wt% NaCl solution for 1 d.

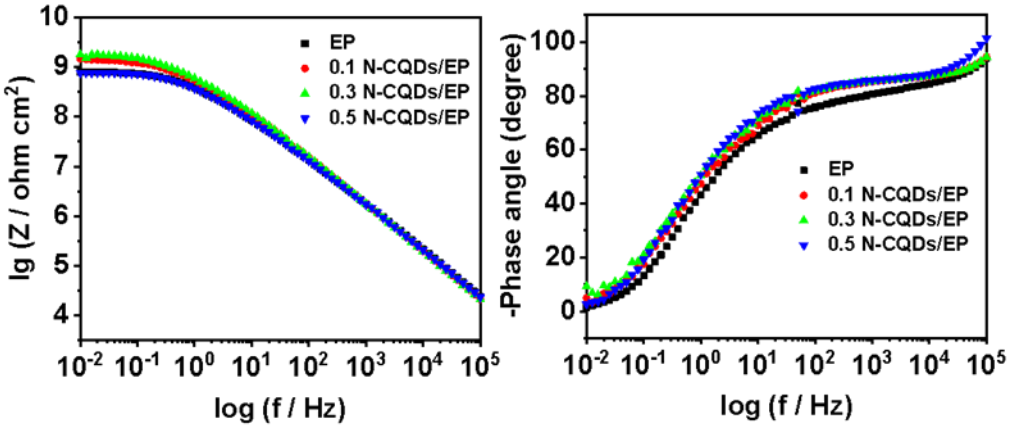

Figure 6. Bode modulus and phase plots of EP and N-CQDs/EP coating on steel immersed in 3.5 wt% NaCl solution for 5 d.

As shown in Fig. 6, the low-frequency impedance values of EP and N-CQDs/EP were still maintained at about 10^9 Ω cm^2 after 5 d immersion. This result indicated that all coatings effectively protect the metal during short-term service. The 0.5 N-CQDs/EP coating on steel impedance value was less than 10^9 Ω cm^2 due to the aggregation of N-CQDs in the coating. In short, agglomeration of N-CQDs decreased the physical barrier of the coating to corrosive media [27]. Interestingly, the low-frequency impedance value of 0.3 N-CQDs/EP coating on steel was similar to 1 d and still more than 10^9 Ω cm^2.

As shown in Fig. 7, the low-frequency impedance values of all N-CQDs/EP coating on steel were maintained at about 10^9 Ω cm^2 at 10 d, and 0.3 N-CQDs/EP coating on steel value became the highest. Compared with Fig. 6, the impedance value of 0.5 N-CQDs/EP coating increased to 10^9 Ω cm^2, which could be explained by the corrosion inhibition of 0.5 N-CQDs in the coating on steel [28]. In this case, N-CQDs could capture water molecules in the coating and temporarily improve the corrosion resistance. Unlike N-CQDs/EP coating on steel, the low-frequency impedance of EP coating on steel dropped to

10^8 Ω cm^2, indicating that pure EP coating on steel was challenging to block the penetration of corrosive media in long-term service. In other words, the corrosion media penetrated into the metal surface, which was also the reason for the change of maximum phase angle (about 90°) between 10^5 to 10^3 Hz.

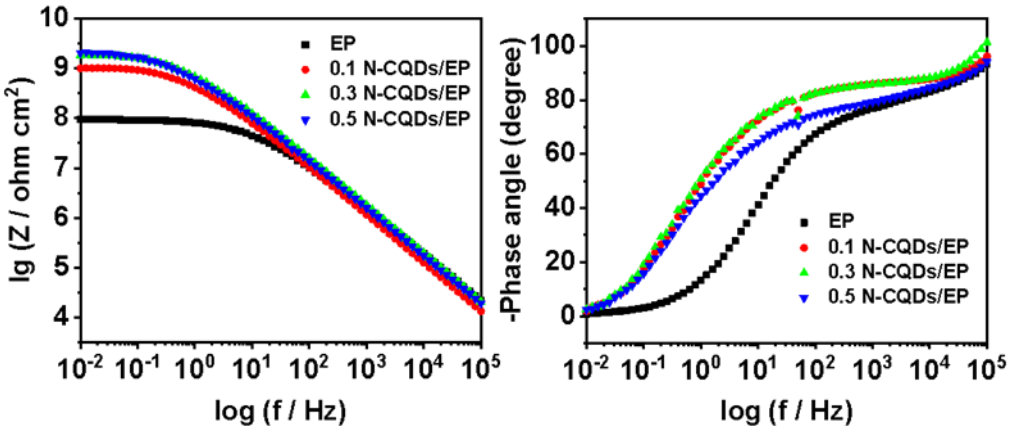

Figure 7. Bode modulus and phase plots of EP and N-CQDs/EP coating on steel immersed in 3.5 wt% NaCl solution for 10 d.

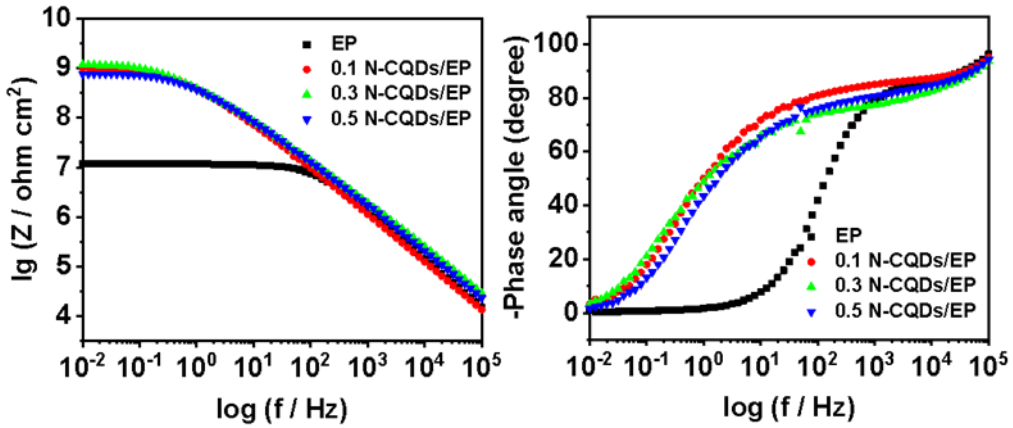

Figure 8. Bode modulus and phase plots of EP and N-CQDs/EP coating on steel immersed in 3.5 wt% NaCl solution for 15 d.

As shown in Fig. 8, all N-CQDs/EP coating on steel low-frequency impedance values were kept at about 10^9 Ω cm^2 at 15 d, while EP coating on steel decreased to 10^7 Ω cm^2. At the same time, the phase angle value of EP reduces significantly at 10^3 Hz. These phenomena indicated that N-CQDs could dramatically improve coating corrosion resistance by enhancing the coating compactness, consistent with the cross-sectional morphologies in Fig. 3.

Similar to Fig. 8, all N-CQDs/EP coating on steel low-frequency impedance values did not change significantly and remained at 10^9 Ω cm^2 in Fig. 9. This phenomenon indicated that N-CQDs could provide reliable protection for Q235 steel in long-term service. Interestingly, the EP coating on

steel impedance values between 15 d and 20 d were similar, related to the protection of corrosion products film on the metal surface [29].

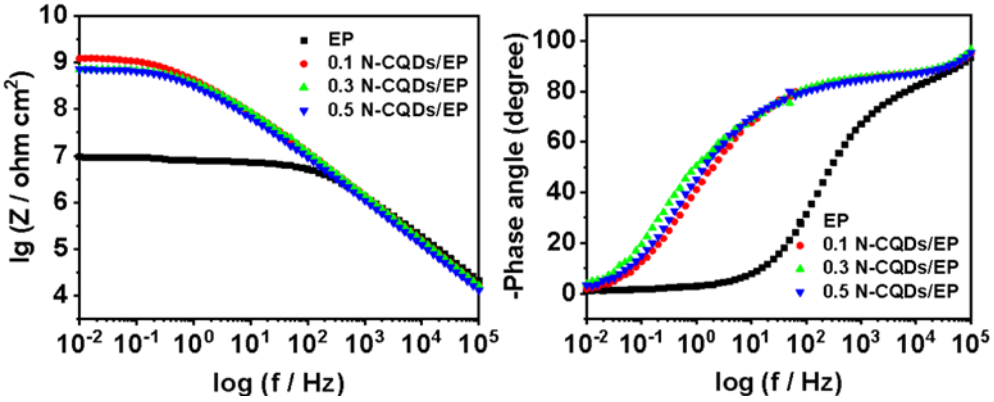

Figure 9. Bode modulus and phase plots of EP and N-CQDs/EP coating on steel immersed in 3.5 wt% NaCl solution for 20 d.

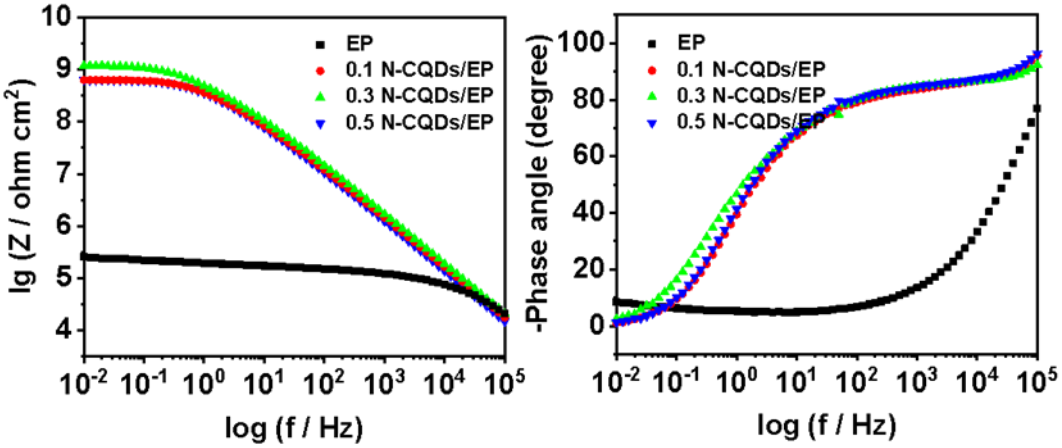

Figure 10. Bode modulus and phase plots of EP and N-CQDs/EP coating on steel immersed in 3.5 wt% NaCl solution for 25 d.

As shown in Fig. 10, low-frequency impedance values of 0.1 N-CQDs/EP and 0.5 N-CQDs/EP were less than 10^9 Ω cm^2, while the value of 0.3 N-CQDs/EP coating on steel was still more than 10^9 Ω cm^2. This result indicated that the coating modification by 0.3 N-CQDs was the most successful and more likely to be applied in the industry. The low-frequency impedance value of EP coating on steel was less than 10^6 Ω cm^2, which implied that the coating had completely lost its ability to protect Q235 steel [30].

After 30 d immersion, all Bode modulus and phase plots of EP and N-CQDs/EP coating on steel were displayed in Fig. 11. It should be noted that the low-frequency impedance values of N-CQDs/EP coating on steel were kept at a high level, which meant that N-CQDs/EP could provide adequate protection for Q235 steel in long-term service. In contrast, the low-frequency impedance value of EP

coating on steel was no more than 10^5 Ω cm^2. Furthermore, the EP phase plot could observe two maximum values (two-time constants). This phenomenon indicated that it was difficult for pure EP coating on steel to maintain long-term corrosion resistance in 3.5 wt% NaCl solution. The excellent anti-corrosion performance of N-CQDs/EP coating on steel could be explained from two sides. On the one hand, the N-CQDs could fill the holes in the coating and enhance coating compactness. On the other hand, the N-CQDs could act as a corrosion inhibitor to adsorb on the steel surface to form a protective film, preventing contact between corrosion media and Q235 steel substrate [31].

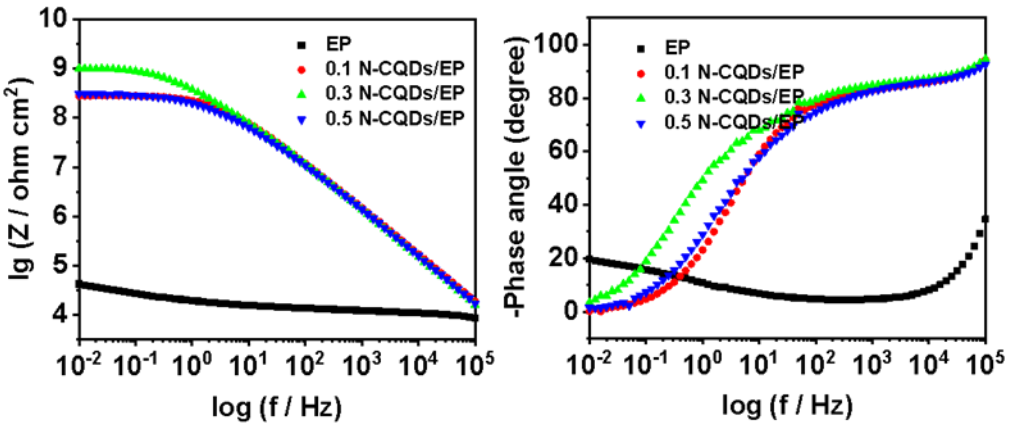

Figure 11. Bode modulus and phase plots of EP and N-CQDs/EP coating on steel immersed in 3.5 wt% NaCl solution for 30 d.

Table 1. Some crucial electrochemical parameters of EP and N-CQDs/EP immersed in 3.5 wt% NaCl solution at various times.

Immersion Time	*Sample*	R_f	R_{ct}	C_f	C_{dl}
(d)	-	(Ω cm^2)	(Ω cm^2)	(μF cm^{-2})	(μF cm^{-2})
1	EP	2.5×10^{8}	8.1×10^{8}	4.2×10^{-10}	4.7×10^{-10}
	0.1 N-CQDs/EP	2.5×10^{9}	2.5×10^{9}	5.0×10^{-10}	1.2×10^{-10}
	0.3 N-CQDs/EP	3.3×10^{8}	4.5×10^{9}	2.9×10^{-10}	4.5×10^{-10}
	0.5 N-CQDs/EP	3.7×10^{9}	1.6×10^{9}	2.9×10^{-10}	5.3×10^{-11}
5	EP	8.2×10^{7}	7.5×10^{8}	5.9×10^{-10}	3.2×10^{-9}
	0.1 N-CQDs/EP	2.2×10^{9}	3.9×10^{9}	7.2×10^{-10}	3.4×10^{-10}
	0.3 N-CQDs/EP	4.6×10^{8}	9.4×10^{8}	1.6×10^{-10}	3.5×10^{-10}
	0.5 N-CQDs/EP	1.4×10^{9}	9.2×10^{8}	2.2×10^{-10}	4.6×10^{-11}
10	EP	7.7×10^{7}	4.5×10^{8}	8.1×10^{-9}	5.8×10^{-9}
	0.1 N-CQDs/EP	3.0×10^{8}	3.5×10^{9}	4.2×10^{-10}	2.3×10^{-10}
	0.3 N-CQDs/EP	5.0×10^{8}	1.1×10^{9}	1.3×10^{-10}	2.8×10^{-10}
	0.5 N-CQDs/EP	8.6×10^{8}	1.7×10^{9}	4.6×10^{-10}	7.3×10^{-10}
15	EP	3.1×10^{7}	9.3×10^{6}	6.6×10^{-9}	6.5×10^{-8}
	0.1 N-CQDs/EP	1.4×10^{8}	1.3×10^{9}	4.5×10^{-10}	9.2×10^{-9}
	0.3 N-CQDs/EP	5.4×10^{8}	8.6×10^{8}	9.6×10^{-9}	2.2×10^{-10}
	0.5 N-CQDs/EP	7.7×10^{8}	2.4×10^{9}	1.4×10^{-10}	4.5×10^{-11}
20	EP	2.5×10^{6}	4.2×10^{6}	3.6×10^{-9}	7.9×10^{-7}
	0.1 N-CQDs/EP	2.9×10^{8}	9.2×10^{8}	4.2×10^{-10}	7.5×10^{-9}

	0.3 N-CQDs/EP	1.4×10^{8}	1.2×10^{9}	1.3×10^{-10}	2.7×10^{-10}
	0.5 N-CQDs/EP	6.8×10^{8}	9.7×10^{8}	4.6×10^{-9}	5.5×10^{-10}
25	EP	3.4×10^{6}	2.2×10^{5}	2.9×10^{-9}	5.3×10^{-6}
	0.1 N-CQDs/EP	2.2×10^{8}	8.0×10^{8}	4.4×10^{-10}	7.9×10^{-9}
	0.3 N-CQDs/EP	1.2×10^{8}	9.5×10^{8}	8.2×10^{-9}	4.3×10^{-9}
	0.5 N-CQDs/EP	5.6×10^{8}	8.1×10^{8}	4.6×10^{-10}	7.6×10^{-11}
30	EP	1.6×10^{4}	2.2×10^{4}	3.6×10^{-9}	4.0×10^{-6}
	0.1 N-CQDs/EP	2.9×10^{8}	8.7×10^{8}	1.6×10^{-11}	5.9×10^{-9}
	0.3 N-CQDs/EP	2.8×10^{8}	8.3×10^{8}	8.8×10^{-9}	5.3×10^{-9}
	0.5 N-CQDs/EP	1.9×10^{8}	8.9×10^{8}	5.4×10^{-9}	4.3×10^{-11}

In order to analyze the corrosion resistance of composite coatings to Q235 steel in detail, some crucial electrochemical parameters were calculated and displayed in Table 1. As shown in Table 1, all coating on the steel was intact, which exhibited high R_f and R_{ct} values. Meanwhile, the C_f and C_{dl} values were low, and the lowest C_{dl} value was 5.3×10^{-11} μF cm^{-2}, indicating 0.5 N-CQDs/EP processed the excellent diffusion resistance ability [32]. With the prolongation of immersion time, the R_f and R_{ct} values of EP decreased faster. After immersion for 30 d, R_f and R_{ct} values were less than 10^5 Ω cm^2, which implied that EP lost the ability to protect steel. Interestingly, the resistance value of composite coating on steel remained at 10^9 Ω cm^2 (30 d), corresponding to their excellent corrosion resistance. On the contrary, the C_f and C_{dl} value of composite coating on steel was still smaller than EP, which indicated that composite coating on steel could effectively inhibit the diffusion of corrosive medium [33].

3.4 Salt spray corrosion

Salt spray corrosion is one of the most common and destructive corrosion behaviors of metals in the marine environment. Therefore, the neutral salt spray test (NSS) is also a simple and effective technique to evaluate the long-term corrosion resistance of coatings. The essential criteria of NSS are the accumulation of corrosion products and the degree of coating swelling.

Before NSS, a 5 cm long scratch was artificially made on the coating surface. Optical photographs of EP and 0.3 N-CQDs/EP coating on steel at different times were given in Fig. 12. As can be seen from the 48 h NSS results, brown rust appeared in EP, and 0.3 N-CQDs/EP coating on steel scratched area, while the corrosive degree was milder in the latter. This phenomenon was attributed to the penetration of aggressive ions (H_2O, O_2, and Cl^-) into the matrix, causing the metal oxidation reaction [34]. With the extension of the NSS test to 72 h, many corrosion products accumulated on EP scratch. Meanwhile, EP coating on steel also swelled and separated from the Q235 steel surface. When the NSS reached 96 h, corrosion media diffusion to metal surface intensified, leading to further fall off of EP. In short, the EP failed to offer protection for Q235 steel. Compared with EP, 0.3 N-CQDs/EP coating on steel showed tinily corrosion products at the scratches, and there was no coating swelling or peeling. This result indicated that N-CQDs played a vital role in composite coatings. When the coating was damaged, N-CQDs could form a shielding film on the Q235 steel surface, inhibiting the diffusion of corrosive media (water, O_2, and Cl^-) [35]. The NSS results were consistent with the electrochemical

impedance data, demonstrating that N-CQDs/EP could improve the long-term corrosion protection of coatings.

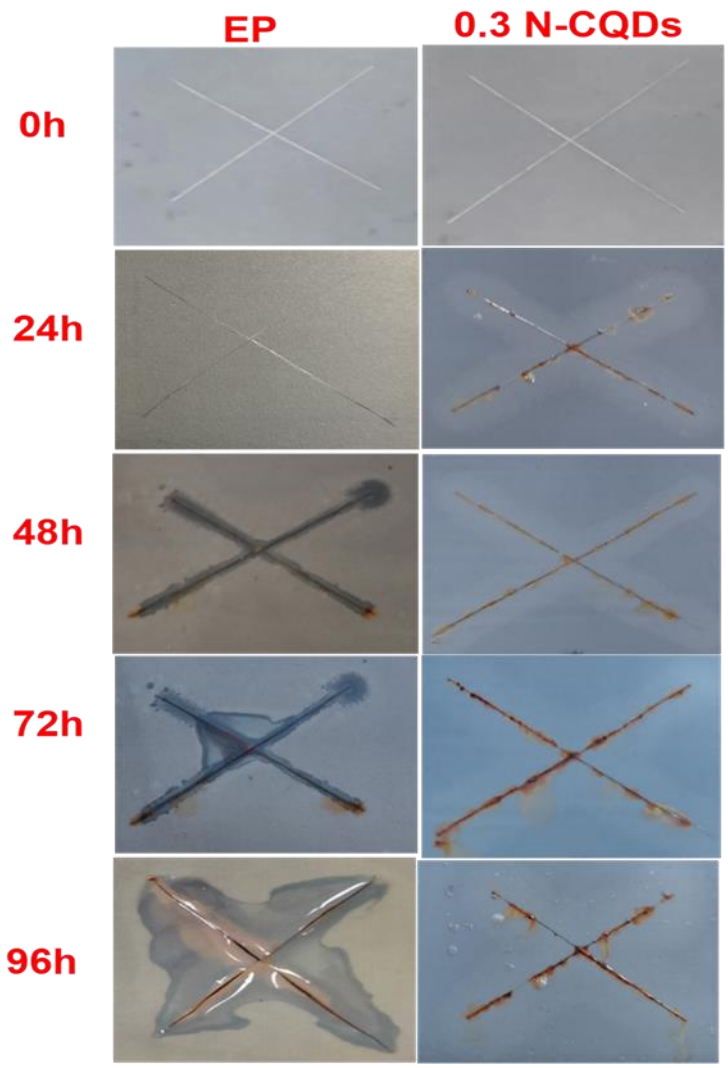

Figure 12. Optical photographs of EP and 0.3 N-CQDs/EP coating on steel under salt spray conditions for different times.

3.5 Mechanical properties

The adhesion force in the coating/substrate interface is one of the key indexes to evaluate the anti-corrosion ability of coatings. As shown in Fig. 13, the adhesion force of pure EP coating on steel was 4.3 MPa, which was the smallest in all test coatings. For the composite coatings on steel, the adhesion force value of 0.1 N-CQDs/EP, 0.3 N-CQDs/EP, and 0.5 N-CQDs/EP was 5.2 Mpa (121%), 6.8 MPa (158%), and 6.2 Mpa (144%), respectively. In other words, N-CQDs nanocomposites could improve the adhesion strength between the epoxy resin and Q235 steel. Moreover, the high adhesion

force between EP/steel meant that the coating was difficult to peel off from the metal surface, which also corresponded to high corrosion resistance.

The mechanism for high adhesion force in N-CQDs/EP coating on steel could be explained from two aspects. On the one hand, carbon quantum dots could form coordination compounds with Fe atoms, improving the bonding force between the coating/steel. On the other hand, N-CQDs could increase the cross-linking density and the physical/chemical interactions of epoxy resin, ultimately improving N-CQDs/EP coating on steel adhesion force.

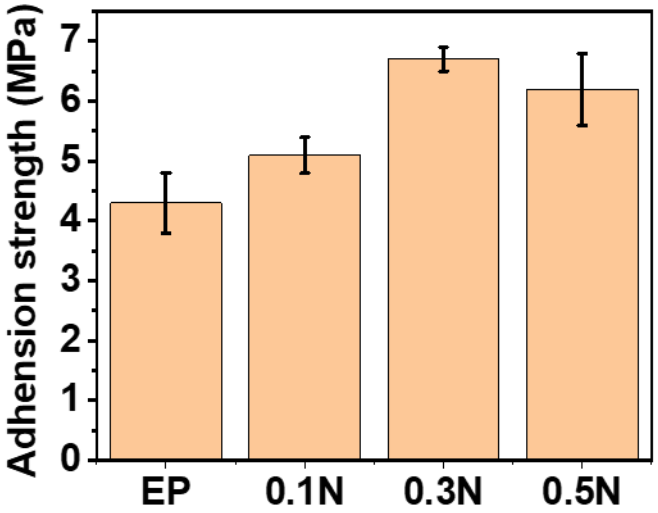

Figure 13. Adhesion force of EP, 0.1 N-CQDs/EP, 0.2 N-CQDs/EP, and 0.5 N-CQDs/EP.

3.6 Fluorescence characteristic of coatings

Biological LSCM investigated the fluorescence characteristic of the coatings under λ=405 nm ultraviolet light. As shown in Fig. 14a, weak fluorescence was detected in the pure EP due to the interaction between the benzene rings in the epoxy resin. With the appearance of N-CQDs in Figs. 14b to d, the fluorescence intensity of the N-CQDs/EP coating on steel was increased, and the phenomenon became evident with the increase of N-CQDs concentrations. This feature might aid in the early detection and prevention of coating cracks [36].

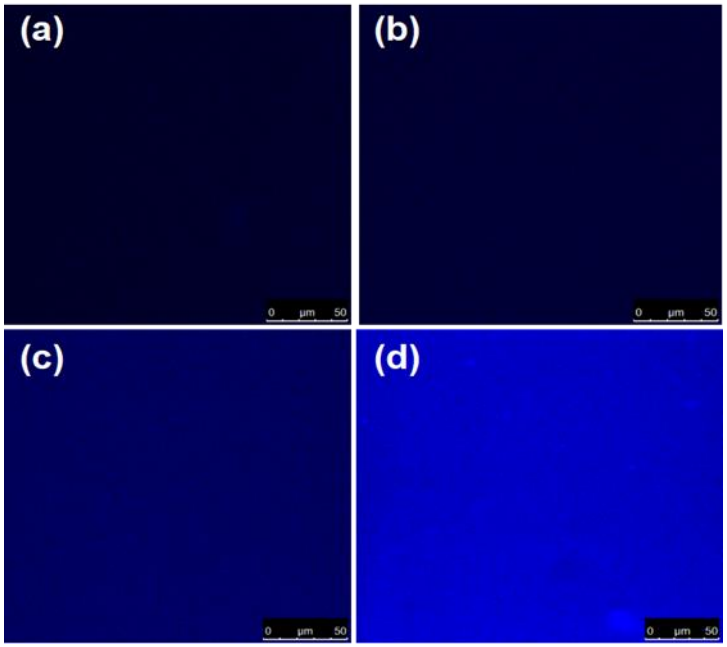

Figure 14. The biological LSCM plots of EP (a), 0.1 N-CQDs/EP (b), 0.2 N-CQDs/EP (c), and 0.5 N-CQDs/EP (d).

3.7 Anti-corrosion of coatings in simulated seawater

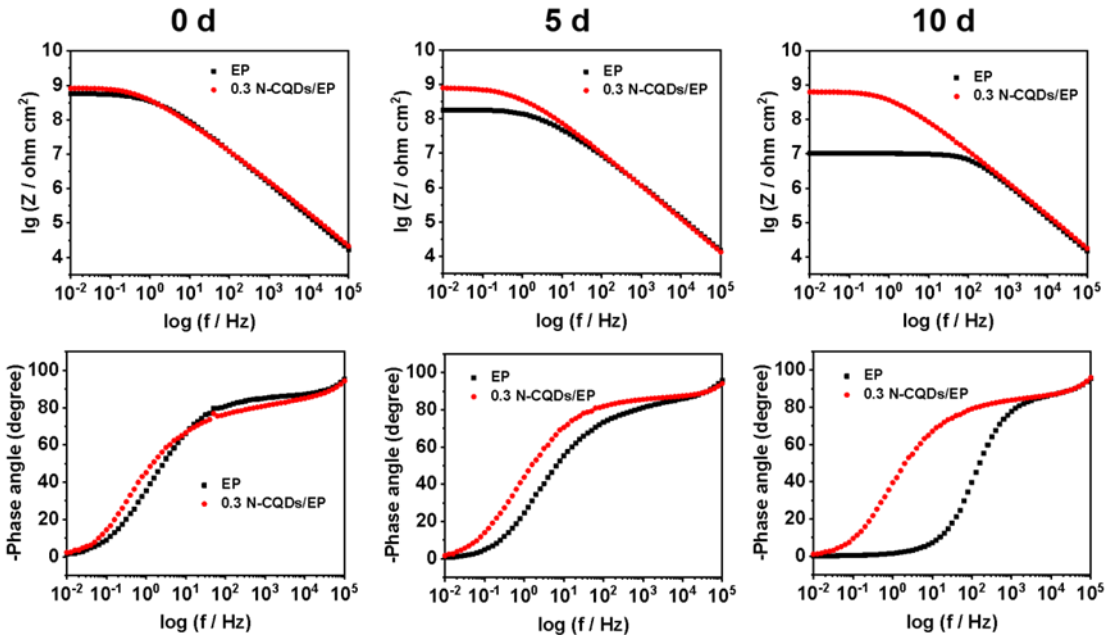

Figure 15. Bode modulus and phase plots of EP and 0.3 N-CQDs/EP immersed in simulated seawater.

EIS tests were carried out on EP and 0.3 N-CQDs/EP coating on steel immersed in simulated seawater to simulate the South China Sea environment. As shown in Fig. 15, the low-frequency impedance value of EP dropped from 10^9 Ω cm^2 to 10^7 Ω cm^2 (about two orders of magnitude) in 10 d, while the impedance reduction of 0.3 N-CQS/EP was slight. In addition, a second time constant appeared

in EP phase angle after immersion for 10 d, indicating that the corrosion media penetrated to steel surface and caused corrosion reactions. In conclusion, 0.3 N-CQDs/EP exhibited excellent corrosion resistance in simulated seawater.

3.8 Corrosion morphology

The SEM and EDS of steel after peeling off EP and 0.3 N-CQDs/EP coating on steel were displayed in Fig. 16. Obvious corrosion pits and products appeared on steel surface after peeling off EP, indicating poor corrosion resistance of the EP. As shown in EDS mapping, the enriched O and Cl elements on the steel surface also demonstrated the unsatisfactory anti-corrosion ability of EP. In other words, the corrosive media diffused to the steel surface, accelerating the corrosion reaction. Interestingly, slight corrosion products were observed on the steel surface protected by 0.3 N-CQDs/EP. Meanwhile, O and Cl elements were not enriched on the steel surface in EDS mapping. These phenomena indicate that 0.3 N-CQDs/EP coating on steel could excellently inhibit the diffusion of corrosive media. This result was consistent with EIS and NSS, meaning 0.3 N-CQDs/EP possessed superior corrosion resistance and impermeability.

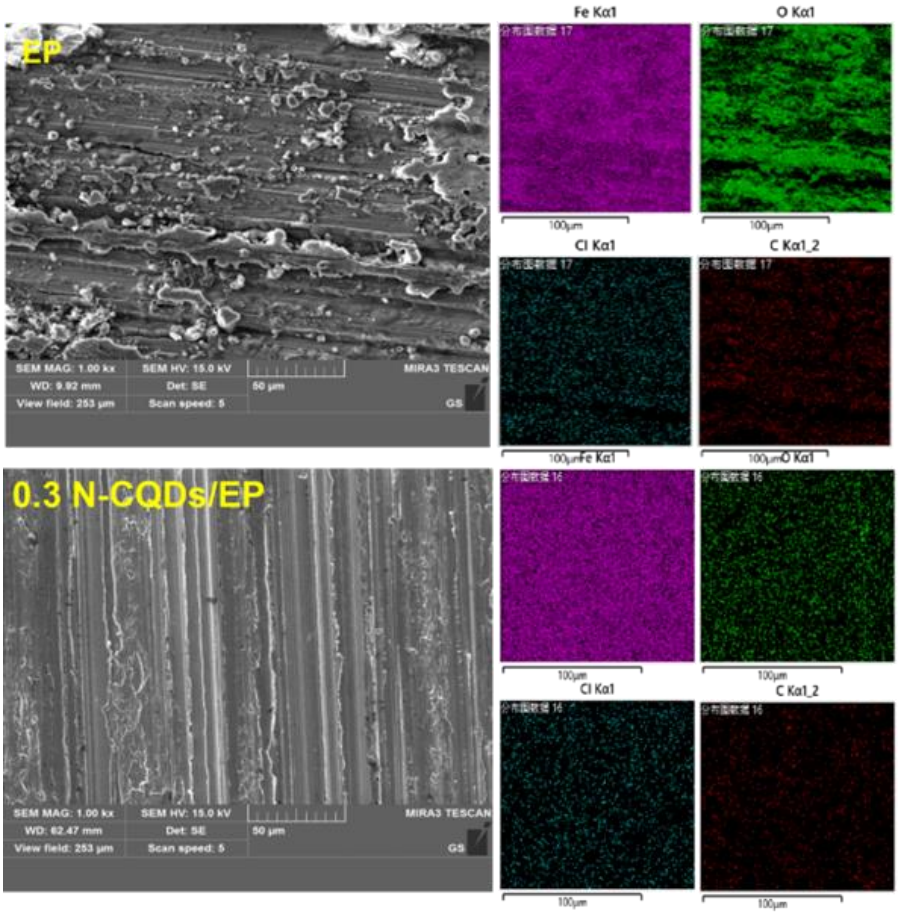

Figure 16. The SEM and EDS of steel after peeling off EP and 0.3 N-CQDs/EP.

4. CONCLUSION

In this work, we synthesized N-CQDs using L-tartaric acid and O-phenylenediamine for the first time. N-CQDs/EP composite coatings on steel were prepared based on N-CQDs and EP. Combining EIS, NSS, adhesion Tester, and LSCM, N-CQDs/EP composite coatings' long-term corrosion resistance, mechanical, and fluorescence properties were studied intensively. The main results were given as follows.

1. The cross-sectional morphologies indicated that N-CQDs could increase the epoxy resin's cross-linking points and density and reduce the pore size of the cross-linking network.

2. Based on the EIS results, the long-term corrosion resistance of N-CQDs/EP was confirmed. At the same time, 0.3 N-CQDs/EP exhibited the best anti-corrosion performance in various composite coatings. The low-frequency impedance value of 0.3 N-CQDs/EP coating on steel was still maintained at about 10^9 □ cm^2 after 30 d immersion.

3. Adhesion tests showed that N-CQDs could significantly improve the adhesion force of the coating, and the highest value was 6.8 MPa. Moreover, the N-CQDs/EP coating on steel fluorescence intensity was increased with the appearance of N-CQDs.

4. N-CQDs/EP also exhibited excellent corrosion resistance in simulated seawater, consistent with EIS results in 3.5 wt% NaCl solution.

References

1. Y. Qiang, S. Zhang, B. Tan, and S. Chen, *Corrosion Science,* 133 (2018) 6-16.
2. Y. Qiang, H. Zhi, L. Guo, A. Fu, T. Xiang, and Y. Jin, *Journal of Molecular Liquids,* 351 (2022) 118638.
3. H. Li, Y.J. Qiang, W.J. Zhao, and S.T. Zhang, *Colloids and Surfaces A,* 616 (2021) 126077.
4. Y. Wu, W. Zhao, S. Liu, and L. Wang, *Chemical Engineering Journal,* 438 (2022) 135483.
5. S. Eid, *International Journal of Electrochemical Science,* 16 (2021) 150852.
6. Y.H. Zhao, K. Wang, X.J. Zhai, M.J. Shi, F.F. Li, C.C. Ye, J.L. Shen, and J. Zhang, *International Journal of Electrochemical Science,* 17 (2022) 220753.
7. H. A. Alrafai, *International Journal of Electrochemical Science,* 17 (2022) 220216.
8. H. Li, S.T. Zhang, and Y.J. Qiang, *Journal of Molecular Liquids,* 321 (2021) 114450.
9. Y. Qiang, L. Guo, H. Li, and X. Lan, *Chemical Engineering Journal,* 406 (2021) 126863.
10. Y. Qiang, H. Li, and X. Lan, *Journal of Materials Science & Technology,* 52 (2020) 63-71.
11. Y. Zhang, Y. Qiang, H. Ren, J. Cao, L. Cui, Z. Zong, D. Chen, and T. Xiang, *Progress in Organic Coatings,* 170 (2022) 106971.
12. J. Wang, L. Ma, Y. Huang, C. Ren, H. Yang, Y. Wang, T. Liu, and D. Zhang, *Composites Part B: Engineering,* 231 (2022) 109574.
13. B. Jiang, Q. Xiang, A. Atrens, J. Song, and F. Pan, *Corrosion Science,* 126 (2017) 374-380.
14. G. Zhang, L. Wu, A. Tang, Y. Ma, G.-L. Song, D. Zheng, B. Jiang, A. Atrens, and F. Pan, *Corrosion Science,* 139 (2018) 370-382.
15. D.A. Winkler, M. Breedon, P. White, A.E. Hughes, E.D. Sapper, and I. Cole, *Corrosion Science,* 106 (2016) 229-235.
16. Y. Wu, F. Jiang, Y. Qiang, and W. Zhao, *Carbon,* 176 (2021) 39-51.
17. M. Schriver, W. Regan, W.J. Gannett, A.M. Zaniewski, M.F. Crommie, and A. Zettl, *Acs Nano,* 7 (2013) 5763-8.
18. J. Ding, H. Zhao, and H. Yu, *ACS Nano,* 16 (2022) 710-720.

19. H. Li, Y. Qiang, W. Zhao, and S. Zhang, *Corrosion Science*, 191 (2021) 109715.
20. J. Wang, L. Ma, X. Guo, S. Wu, T. Liu, J. Yang, C. Ren, S. Li, and D. Zhang, *Chemical Engineering Journal*, 433 (2022) 134515.
21. Y. Qiang, S. Zhang, H. Zhao, B. Tan, and L. Wang, *Corrosion Science*, 161 (2019) 108193.
22. S. Ren, M. Cui, X. Chen, S. Mei, and Y. Qiang, *Journal of Colloid and Interface Science*, 628 (2022) 384-397.
23. L. Shen, S. He, W. Xie, L. Miao, J. Liu, H. Zhou, B. Li, and Y. Qiang, *Progress in Organic Coatings*, 172 (2022) 107148.
24. S. Qiu, Y. Su, H. Zhao, L. Wang, and Q. Xue, *Corrosion Science*, 178 (2021).
25. C.X. Zhao, J.X. Wei, J.J. Wu, Y.T. Li, D. Xiang, Y.P. Wu, H. Li, and Z.R. Hou, *International Journal of Electrochemical Science*, 17 (2022) 220627.
26. Y. Qiang, S. Zhang, S. Xu, and W. Li, *Journal of Colloid and Interface Science*, 472 (2016) 52-59.
27. Y. Qiang, S. Zhang, and L. Wang, *Applied Surface Science*, 492 (2019) 228-238.
28. H. Li, S. Zhang, B. Tan, Y. Qiang, W. Li, S. Chen, and L. Guo, *Journal of Molecular Liquids*, 305 (2020) 112789.
29. P. Najmi, N. Keshmiri, M. Ramezanzadeh, and B. Ramezanzadeh, *Chemical Engineering Journal*, 412 (2021) 128637.
30. A. Dehghani, G. Bahlakeh, and B. Ramezanzadeh, *Chemical Engineering Journal*, 400 (2020) 125860.
31. Y. Qiang, S. Fu, S. Zhang, S. Chen, and X. Zou, *Corrosion Science*, 140 (2018) 111-121.
32. Q. Xiang, Y. Qiang, and L. Guo, *Progress in Organic Coatings*, 174 (2023) 107293.
33. X. Yao, Y. Qiang, L. Guo, Q. Xu, L. Wen, and Y. Jin, *Journal of Industrial and Engineering Chemistry*, 114 (2022) 427-437.
34. M. Zhang, F. Xu, D. Lin, J. Peng, Y. Zhu, and H. Wang, *Chemical Engineering Journal*, 446 (2022) 137078.
35. J. Ding, H. Zhao, and H. Yu, *Chemical Engineering Journal*, 430 (2022) 132838.
36. C. Liu, H. Wu, Y. Qiang, H. Zhao, and L. Wang, *Corrosion Science,* 184 (2021) 109355